

bradscholars

Lanthanide (Er, Eu)-Doped TiO₂ with Enhanced Kinetics for a High-Performance Asymmetric Supercapacitor and Oxygen Evolution Reaction

Item Type	Article
Authors	Hussain, M.N.;Naveed, A.;Sohail, M.;Khan, M.D.;Hickey, Stephen;Ullah, N.;Ahmad, I.;Haider, A.;Shah, S.M.
Citation	Hussain MN, Naveed A, Sohail M et al (2025) Lanthanide (Er, Eu)-Doped TiO ₂ with Enhanced Kinetics for a High-Performance Asymmetric Supercapacitor and Oxygen Evolution Reaction. ACS Applied Engineering Materials. 3(5): 1315-1326.
DOI	https://doi.org/10.1021/acsaenm.5c00121
Publisher	ACS
Download date	2026-04-12 08:50:17
Link to Item	https://bradscholars.brad.ac.uk/handle/10454/20786.2

Lanthanide (Er, Eu) Doped TiO₂ with Enhanced Kinetics for High-Performance Asymmetric Supercapacitor and Oxygen Evolution Reaction

Muhammad Nasir Hussain^{a*}, Abdul Naveed^a, Muhammad Sohail^b, Malik Dilshad Khan^c,
Stephen G Hickey^d, Naimat Ullah^a, Iqbal Ahmad^b, Ali Haider, Syed Mujtaba Shah^{a*}

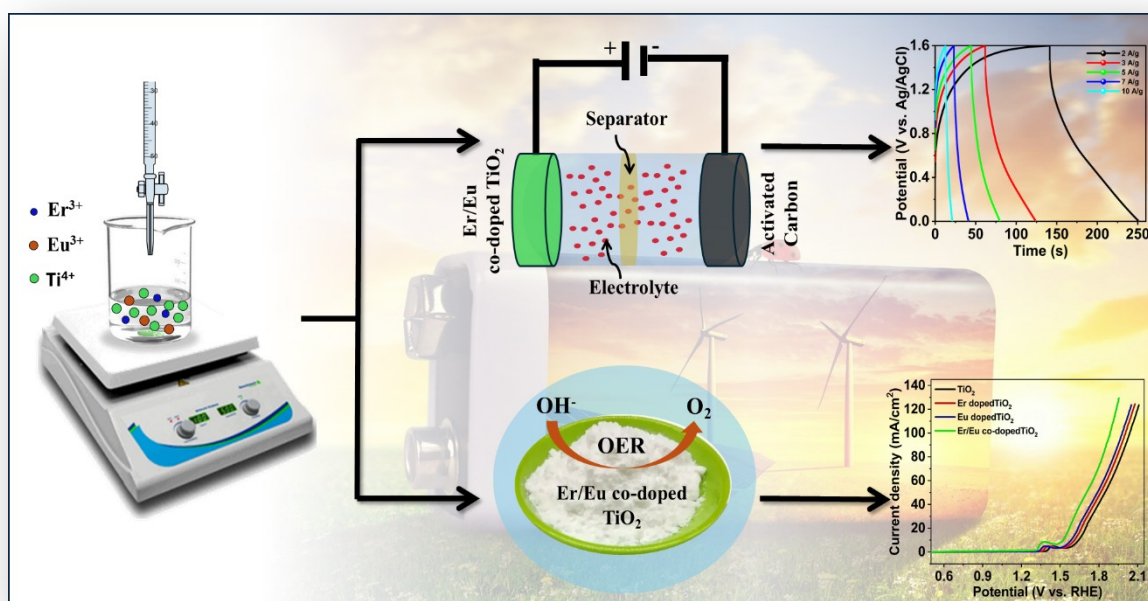
^aDepartment of Chemistry, Quaid-i-Azam University, Islamabad, 45320, Pakistan.

^bDepartment of Chemistry, Allama Iqbal Open University, Islamabad, 44000, Pakistan

^cDepartment of Chemistry, University of Zululand, Private Bag X1001, KwaDlangezwa, 3880, South Africa.

^dSchool of Chemistry and Biosciences, University of Bradford, BD7 1DP, United Kingdom.

Graphical Abstract:



Abstract:

Supercapacitor performance is generally hindered by sluggish electrode reaction kinetics, which can be improved through doping to create surface defects, oxygen vacancies, and active sites. Pristine TiO₂, Er-doped, Eu-doped, and Er/Eu co-doped TiO₂ nanoparticles were synthesized via a solution-based method. Among all of the electrodes fabricated, Er/Eu co-doped TiO₂ showed the highest specific capacitance of 1772.5 F g⁻¹ at 1 A g⁻¹ and a low charge transfer resistance of 12.37 Ω, highlighting the enhanced electrical conductivity and rapid ion and electron transport. The Er/Eu co-doped TiO₂ electrode was further investigated in asymmetric supercapacitor geometry where it demonstrated a wide potential window of 1.6 V and specific capacitance of 135 F g⁻¹ at 2 A g⁻¹, energy density of 48 Wh kg⁻¹, and power density of 1.6 kW kg⁻¹. Additionally, TiO₂, Er-doped, Eu-doped and Er/Eu co-doped TiO₂ exhibited excellent oxygen evolution reaction performance, with onset potentials of 1.57, 1.52, 1.49, and 1.47 V and low overpotentials of 460, 400, 380 and 290 mV at 20 mA cm⁻². The electrodes exhibited excellent electrochemical stability when tested for 20 hours using constant potential electrolysis. Tafel slopes of 166.11, 164.71, 139.08 and 115.19 mV dec⁻¹, suggested that all the electrocatalysts under study are promising materials for OER research. These findings confirm that TiO₂ co-doped with rare earth metals is an appealing electrode material for energy storage as well as energy generation.

Keywords: Lanthanide doping, Electrode kinetics, Battery-type supercapacitors, OER activity, Titania.

Introduction

The exponential increase in the use of fossil fuels due to industrialization and urbanization, has led to the depletion of their reserves and has had a detrimental impact on the environment.¹ There is therefore an urgent need to develop alternative environmentally friendly, affordable, and sustainable energy technologies, capable of meeting the global energy demand while curbing society's reliance on fossil fuels.²⁻⁵ The resulting reduction in the use of fossil fuels will also assist to mitigate global warming. In this regard, efforts are being devoted to advancing both renewable energy generation and energy storage technologies. According to the statistical data, the demand for energy storage devices (ESDs) will increase threefold by 2030 compared to their current value.⁶⁻⁷ Recently, ESDs have become indispensable in our lives and are used in a wide range of products, such as portable devices, mobile phones, computers, and hybrid electric vehicles,⁸⁻⁹ to name just a few. Among commonly used energy storage devices, supercapacitors (SCs) offer numerous advantages such as safe operation, high power density, rapid charge/discharge rates, and long-life cycles compared to batteries. SCs have been demonstrated to possess a maximum efficiency of 98% surpassing that of batteries which exhibit between 70 and 95% with respect to their power density. SCs exhibit power densities in the range of 1000–2000 W kg⁻¹ whereas batteries are typically in the range from 50–200 W kg⁻¹, with the life cycle of SCs exceeding 1,000,000 cycles due to their fast charge-discharge rate.¹⁰⁻¹² SCs store charge through two mechanisms depending on the electrode material type employed. Carbon-based materials utilize the electrical double-layer capacitance (EDLC) at the electrode-electrolyte interface, while metal oxides and polymers employ pseudocapitance via faradaic reactions.¹³⁻¹⁴ Therefore, development of electrode materials exhibiting exceptional electrochemical properties is essential. Metal oxides such as MnO₂, NiO, RuO₂, V₂O₅, TiO₂, and Co₃O₄, as well as a number of conducting polymers, have shown potential for application as SC electrodes.¹⁵⁻¹⁸ While metal oxides exhibit high specific capacitance they often suffer from poor charge-discharge rates and stability, a condition which can be improved through doping and composite formation.¹⁹

TiO₂ has gained huge attraction as an electrode material in SCs because of its low toxicity and excellent stability.²⁰⁻²¹ TiO₂ exists in three phases: rutile, anatase, and brookite, with each having unique structural properties.²² The anatase phase stands out as the most stable phase of TiO₂ when its dimensions are on the nanoscale.²³ Numerous strategies such as doping with metals or non-metals and creating surface defects/oxygen vacancies, have proven to be useful in modifying surface properties.²⁴⁻³² Therefore, various strategies for the modification of TiO₂

for energy storage applications have been made. Recently, Jaffri et al.³³ prepared a lanthanide-doped TiO₂ system (Ce/Pr/Nd)³⁺ with excellent bifunctionality for water splitting (OER: 140 mV, HER: 135 mV), high capacitive performance (749 F g⁻¹), and low resistance (0.12 Ω). Additionally, the material served as an efficient electron transport layer in perovskite solar cells, achieving 16.71% efficiency under ambient conditions. Munawar et al.³⁴ developed Ce/Ho co-doped TiO₂ nanostructures synthesized via a sol-gel method which showed a high specific capacitance of 1714 F g⁻¹ and 99.28% capacity retention after 5,000 cycles. Li et al.³⁵ synthesized a 3D N-doped Ti₃C₂/TiO₂ hollow composite which exhibited a high capacitance of 572 F g⁻¹ and 99.6% stability over 9,500 cycles. When employed in a symmetric supercapacitor device it achieved a capacitance of 157 F g⁻¹ and an energy density of 17.7 Wh kg⁻¹, demonstrating excellent energy storage potential. Lanthanides have been used as dopants in various materials in order to tune their structural, optical, electronic, and magnetic properties.³⁶⁻⁴¹ With respect to supercapacitor applications in particular, the doping of Er and Eu in various metal oxides has shown multifold enhancements in their charge storage capacity and cyclic stability.⁴²⁻⁴⁶ The presence of 4f unpaired electrons in Er and Eu contributes to enhancing the energy storage capacity of the materials as the electrons do not participate in chemical bonding. Additionally, rare earth metals are considered to be chemically passive and many form redox couples which indicates the thermodynamic feasibility of electrochemical storage.⁴⁷ In comparison to single metal doping, the co-doping of metal oxides creates additional defects and oxygen vacancies, improving electrical conductivity and enriching active sites. This modification leads to enhanced reaction kinetics, generating a synergistic effect that ultimately increases the overall energy storage capacity of the materials.⁴⁸

In addition to charge storage devices, researchers are also focusing their efforts on the development of low-cost, efficient and stable electrocatalysts to be used as an alternative to expensive noble metal-based catalysts. Thus, it is imperative to design cutting-edge materials with exceptional electrochemical properties.⁴⁹ TiO₂ is also a promising electrocatalyst owing to its low overpotential and high electrochemical stability when employed for water electrolysis.⁵⁰⁻⁵¹ Moreover, rare earth metal-doped TiO₂ nanomaterials have proven to be excellent electrocatalysts with enhanced efficiency, particularly in oxygen evolution reaction (OER), offering a viable solution for the development of renewable and sustainable electrocatalysts.⁴⁸ During the OER, one component may act as a co-catalyst for other components present within the system. In situ generated MOOH (M = metal) behaves as a co-

catalyst to elevate the catalytic performance of the OER catalyst. The positively charged MOOH absorbs oxygen while the negatively charged metal oxide (TiO_2) absorbs the hydrogen atoms of the water molecules. This collaborative effect between MOOH and TiO_2 accelerates the cleavage process of H–OH into H_2 and O_2 gases at their respective electrodes during the water splitting process. Under strongly alkaline conditions, the transition metal oxides often oxidize to their corresponding oxides/(oxy)hydroxides at the operation potentials at which the OER occurs. Surprisingly, the species formed after the transition metal oxide autoxidation exhibit greater catalytic activities towards OER compared to its pre-oxidized catalytic performance.

Herein, we present a facile synthesis of pristine, Er-doped, Eu-doped, and Er/Eu co-doped TiO_2 nanoparticles by using a simple solution based chemical method. The effect of mono- and co-doping TiO_2 with lanthanides on the charge storage performance was investigated in a three-electrode system as well as by fabricating an asymmetric device. In addition, the bifunctionality/versatility of the synthesized materials was examined by employing them to perform the electrochemical OER. Overall, doping TiO_2 with lanthanides has proven to be a very useful strategy for improving the process of bifunctional energy generation and storage.

Experimental Section

Materials

The titanium(IV) tetra isopropoxide ($\text{Ti}[\text{OCH}(\text{CH}_3)_2]_4$, 97%), erbium nitrate ($\text{Er}(\text{NO}_3)_3 \cdot 5\text{H}_2\text{O}$, 99.9%), europium nitrate ($\text{Eu}(\text{NO}_3)_3 \cdot 5\text{H}_2\text{O}$, 99.9%), and 1-propanol were purchased from Sigma Aldrich and used as received.

Synthesis of Pristine and Co-doped TiO_2 Nanoparticles

In a typical synthesis, titanium(IV) tetraisopropoxide (TTIP) (3.25 mL) was mixed with 1-propanol (7.8 mL) and stirred for 10 minutes. A mixture of de-ionized water (0.8 mL) and 1-propanol (4.9 mL) was added dropwise to the above solution. Subsequently, the mixture was left to stir for 24 hours at room temperature. The resulting mixture was then centrifuged and dried at room temperature overnight. The powder obtained was annealed at 500 °C for 1 hour. The doped and co-doped 5% (Er, Eu) TiO_2 nanoparticles were synthesized by employing the same procedure except the dopant salts were added to the 1-propanol before the addition of TTIP. The resulting powder was again dried and subsequently annealed at 500 °C for 1 hour to obtain mono- and co-doped TiO_2 nanoparticles. The synthesis scheme for Er/Eu co-doped TiO_2 is shown in **Figure 1**.⁵²

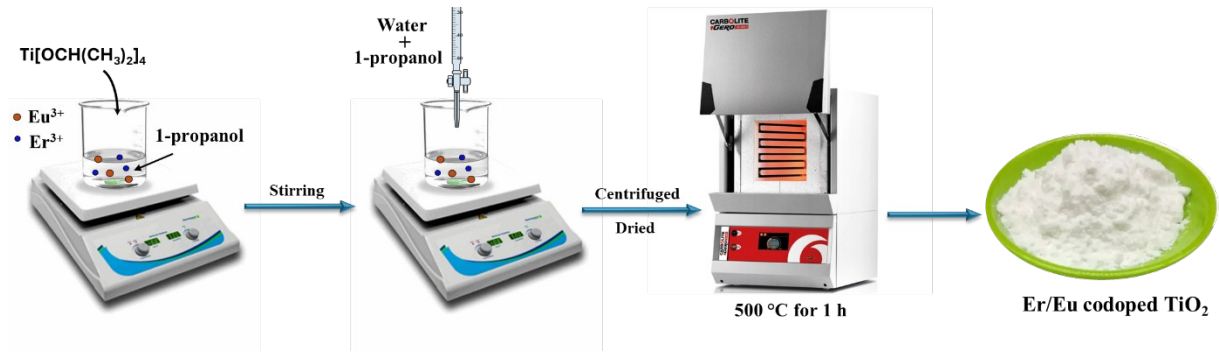


Figure 1. illustration for the synthesis of Er/Eu co-doped TiO_2

Preparation of Polymer Gel Electrolyte

PVA/KOH gel polymer electrolyte was used as separator for the fabrication of a quasi-solid-state device. Synthesis of the separator was accomplished through a solution-casting method. Briefly, 1.5 grams of PVA was added to 20 mL of distilled water, and the mixture agitated at 90 °C until it became clear and uniformly viscous. Following the cooling of the solution to ambient temperature, 10 mL of an aqueous solution containing 2 g of KOH was slowly introduced while ensuring continuous stirring for 2 hours at room temperature. The resultant transparent, adhesive solution was then transferred into a petri dish and allowed to remain undisturbed for 24 hours to facilitate the spontaneous drying of the polymer.

Electrode Fabrication and Measurement

The working electrodes were fabricated by depositing the active materials onto activated nickel foam. The activation of nickel foam was achieved by washing it with acetone, 3 M H_2SO_4 , water and ethanol, respectively. The thick slurry-like paste was made by dissolving 80% synthesized active materials, 10% conducting carbon, and 10% polyvinylidene fluoride (PVDF) in N-methyl-2-pyrrolidone (NMP). The as-prepared slurry was drop-cast onto the activated nickel foam having dimensions $1 \times 1 \text{ cm}^2$ and dried at 70 °C for 12 hours. The mass loading of the active material was approximately $1 \text{ mg} \pm 5\%$. The mass was calculated before and after the deposition on nickel foam. The electrochemical measurements were performed on a Gamry workstation (interface 1010E). Asymmetric devices were fabricated by the same method with the exception that the dimensions were $1.5 \times 1.5 \text{ cm}^2$. Specific capacitance (C_{sp}) values were evaluated by employing equation 1 and 2 for the three-electrode setup and fabricated device.⁵³

$$C_{sp} = \frac{\int IdV}{2 km \Delta V} \quad (1)$$

$$C_{sp} = \frac{I \Delta t}{m \Delta V} \quad (2)$$

where C_{sp} is in $F g^{-1}$, I denotes current (A), m the mass in grams, Δt the discharge time in seconds, and ΔV the potential window in volts.

For electrochemical OER investigations, the following equations have been used.

$$E_{RHE} = E_{Ag/AgCl} + (0.1976 + 0.059 \text{ pH}) \text{ V} \quad (3)$$

$$\eta = E_{RHE} - 1.23 \text{ V} \quad (4)$$

The Nernst equation has been employed to calibrate all potential values. While the 0.1976 V is the standard potential of the Ag/AgCl electrode at 25°C and 0.059 V demonstrates the Nernstian slope, which adjusts for the effect of pH on the potential. The 1.23 V is the theoretical minimum voltage required to split water into hydrogen and oxygen under standard conditions. The kinetic parameters were evaluated by using the Tafel equation.

$$\eta = b \log(j) + a \quad (5)$$

The value of b can be found from the slope, j represents the current density, and a is a constant which may be determined from the intercept of the line with the y-axis.⁵⁴

The double layer capacitance (C_{dl}) was measured by using CV in the non-faradic window, between -50 to 150 mV against the Ag/AgCl reference electrode, at different scan rates ranging from 5 to 50 mV/s. Thereafter, the electrochemically active surface area (ECSA) was calculated using the following equation 6.

$$ECSA = C_{dl} / C_{sp} \quad (6)$$

where C_{sp} is the specific capacitance of the materials. The turnover frequency (TOF) is calculated using the following equation 7.

$$TOF = I / (4 \times F \times m) \quad (7)$$

where I is current, F is the Faraday constant and m the number of moles of catalyst used during the electrolysis experiment.

Physical Characterization with Methods of Preparation

The X-ray diffraction (XRD) spectra were obtained using a Bruker advance AXS D8 diffractometer with a Cu source running at 30 kV and 10 mA. The as-prepared samples were placed on a silicon wafer holder. Raman spectra were obtained on the Renishaw InVia instrument using an excitation laser whose wavelength was 633 nm. The samples were loaded on a thin Al film and the laser power was maintained below 0.02 mW. The optical studies

were carried out with the aid of a UV-visible (Shimadzu-1700) double beam spectrophotometer. The materials were first dispersed in water and then stored for 2 hours before obtaining the spectra. Scanning electron microscopy (SEM) images were conducted on an FEI Quanta 400, equipped with an Oxford Instruments Xplore 30 energy dispersive spectroscopy (EDS) detector. The as-prepared samples were deposited onto Al stubs followed by sputtering with a carbon layer. The energy dispersive X-ray spectroscopy (EDX) and elemental mapping were recorded simultaneously on the same instrument. Transmission electron microscopy (TEM) images were captured on a JEOL JEM-1200 EX MKII microscope, equipped with a thermionic gun (tungsten filament), operating at an acceleration voltage of 120 kV. The as-prepared samples were dispersed in water and dropped onto carbon-coated copper grids followed by solvent evaporation.

Results and Discussion

The phase formation and purity of the pristine and modified nanomaterials were elucidated by XRD as shown in **Figure 2(a)**. The peaks precisely align with those of the anatase phase of TiO_2 (ICDD # 83-2243) and can be indexed to the (101), (004), (200), (105), (211), and (204) planes, respectively. However, there was a negligibly small/minor peak around $\approx 31^\circ$ that matches with the brookite phase of TiO_2 (indexed as (121)). The position of the diffraction peaks remains the same after the addition of dopants, however their intensity varies. The lanthanide (Er or Eu) doping did not induce any phase change in the TiO_2 crystal structure or other impurity phases, and no noticeable shift in peak positions was observed, probably due to very low dopant concentration. Raman analysis was carried out to further explore the structural properties of the synthesized materials as shown in **Figure 2(b)**. Pristine TiO_2 showed four main bands at 635.12 cm^{-1} , 526.92 cm^{-1} , 407.73 cm^{-1} , 152.68 cm^{-1} which can be assigned to E_g , B_{1g} , A_{1g} , and asymmetric stretching modes, respectively.⁵⁵ The variations in the intensities of the bands are due to different factors such as particle size, concentration, oxygen vacancies, and structural defects.⁵⁶ No change occurred after the doping and co-doping which suggests the successful incorporation of dopants and attests to the phase purity of TiO_2 nanoparticles. The optical behavior of the prepared materials was analyzed from which it could be observed that the maximum absorption for pristine TiO_2 nanoparticles lies at 261 nm. Doping of Er and Eu into the TiO_2 structure shifts the absorption to longer wavelengths of 273 nm and 284 nm, respectively. The absorption maxima for Er/Eu co-doped TiO_2 nanoparticles shifted even further to a wavelength of 298 nm as displayed in **Figure 2(c)**. The band gaps of pristine TiO_2 , Er-doped, Eu-doped, and Er/Eu co-doped TiO_2 nanoparticles, as estimated by Tauc plot, showed estimated band gap values of 3.21 eV, 3.13

eV, 3.03 eV, and 2.91 eV, respectively (**Figure 2(d)**). Additionally, Er and Eu ions have a very strong binding affinity to oxygen atoms, therefore, these ions can scavenge oxygen atoms and create oxygen vacancies at the surface of TiO₂, which results in the red shift in the absorption spectra.⁵⁷⁻⁵⁸ These oxygen vacancies have proven to be beneficial for the charge storage capacity of prepared materials.

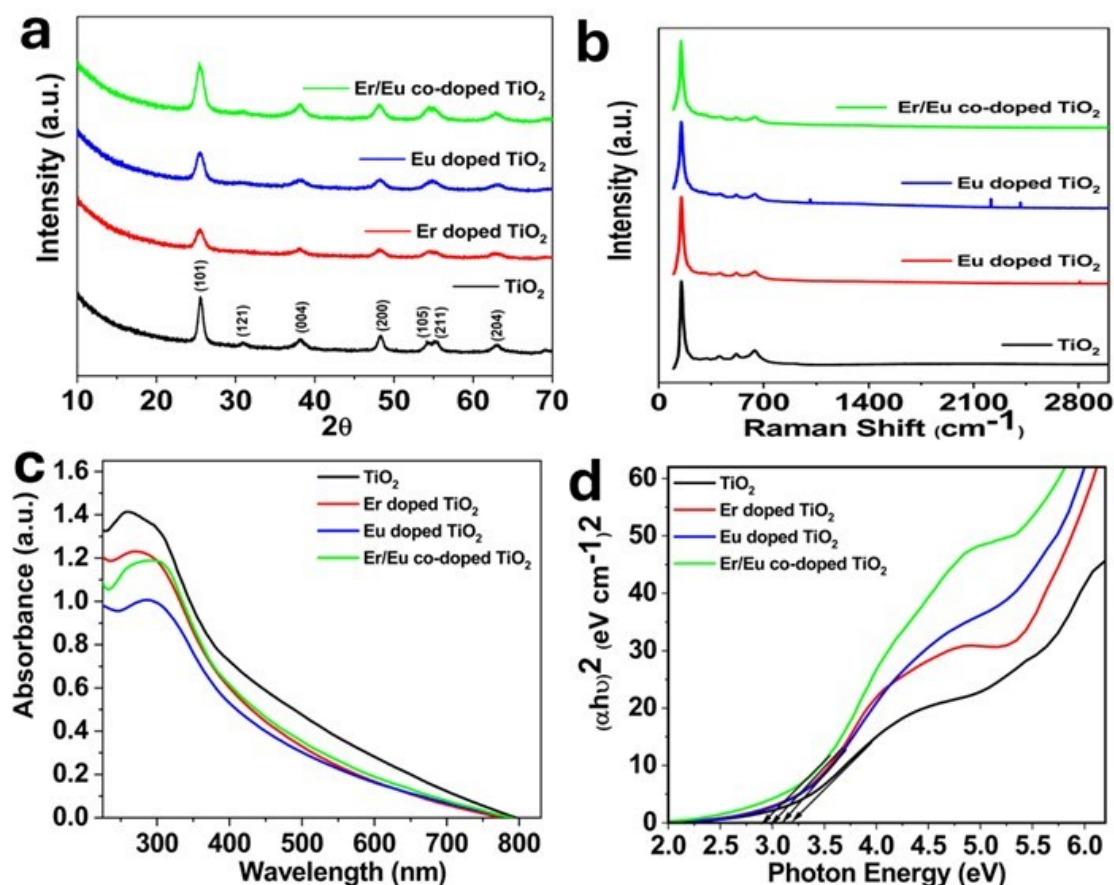


Figure 2. (a) PXRD patterns, (b) Raman spectra, (c) UV-Vis profiles, and (d) Tauc plots of pristine TiO₂, Er-doped TiO₂, Eu-doped TiO₂, and Er/Eu co-doped TiO₂ nanoparticles.

Figure 3(a, b, c, d) displayed the surface morphology of the pristine, doped, and co-doped TiO₂ materials, analyzed by SEM, from which spherically shaped particles agglomerated together can be discerned. No significant change was observed in the shape of the TiO₂ particles after doping or co-doping with Er and Eu, due to the small dopant concentrations. The elemental composition and purity were further investigated by energy dispersive X-ray (EDX) analysis as in **Figure S1**. Prominent signals for Ti, O, Er, and Eu, were observed in the spectra confirming that the materials are indeed composed of Er/Eu co-doped TiO₂. TEM analysis was employed to examine more precisely the size and shape of the as-synthesized pristine, doped, and co-doped materials as presented in **Figure 3(e, f, g, h)**. The TEM images

also confirmed the formation of small spherically shaped nanoparticles having a diameter in the range of 10-15 nanometers, and that no significant change in morphology occurred after doping. Additionally, the electrochemically active surface area has been calculated to determine the active surface of the prepared Er/Eu co-doped TiO₂ electrocatalyst. The ECSA for this electrocatalyst is found to be 2.023 cm⁻². Likewise, the distribution of each element present in the materials was confirmed by elemental mapping which demonstrates the homogeneous distribution of each element as depicted in the images in **Figure 3(i)**.

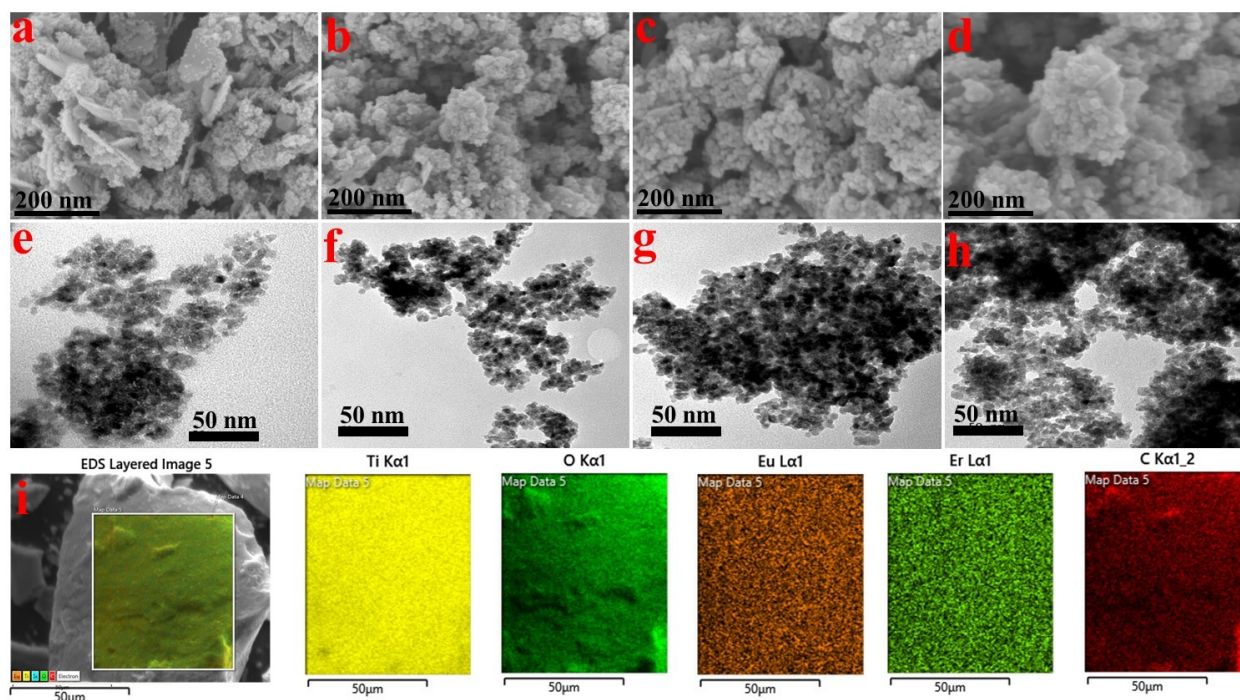


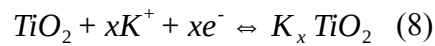
Figure 3. (a, b, c, d) SEM images, (e, f, g, h) TEM images of pristine TiO₂, Er-doped TiO₂, Eu-doped TiO₂, and Er/Eu co-doped TiO₂ nanoparticles, (i) EDS mapping of the Er/Eu co-doped TiO₂ nanoparticles overlaid onto the images of each electrocatalyst material.

Electrochemical Investigations

The optimization of Er/Eu co-doped TiO₂ fabricated electrodes was carried out using CV in 2 M LiOH, 2 M NaOH, and 2 M KOH as electrolyte as presented in **Figure S2(a)**. The prominent redox peaks and maximum area under the CV curves were observed to be greatest in 2 M KOH electrolyte, demonstrating that KOH is the better potential electrolyte of the three, from the point of view of the signal magnitudes, for further investigations. It is important to mention that Li⁺, Na⁺, and K⁺ form hydrated ions in solution. Specifically, K⁺ forms a smaller hydrated ionic radius of 3.31 Å which offers a smaller solution resistance while Li⁺ and Na⁺ have hydrated ionic radii of 3.58 Å and 3.82 Å, respectively. These hydrated ionic radii have a significant influence on the electrochemical performance of the

materials.⁵⁹ Er/Eu co-doped TiO₂ nanoparticles have shown the highest specific capacitance in KOH electrolyte compared to other fabricated electrodes and trial electrolytes (NaOH, LiOH).

To compare the electrochemical performance of the fabricated electrodes and bare nickel foam, their specific capacitance was calculated using equation 1 by recording CV profiles at 10 mV/s as shown in **Figure S2(b)**.⁶⁰ The areas under the CV curve for pristine TiO₂, Er doped TiO₂, Er doped TiO₂, and Er/Eu co-doped TiO₂, are 0.00491, 0.00786, 0.01277, and 0.01406 AV with corresponding C_{sp} values of 613.75, 982.50, 1596.25 and 1757.50 F g⁻¹, respectively. To further investigate the effect of scan rate, CV curves were obtained at various scan rates in the range of 10 to 100 mV s⁻¹ as depicted in **Figure 4(a, b, c, d)**. The prominent redox peaks indicate the presence of faradaic reactions that take place at the electrode-electrolyte interface due to the reversible redox chemistry of Ti⁺⁴/Ti⁺³,⁶¹ and the consistent behavior of the curves over many cycles shows the excellent stability of the fabricated electrodes as well as fast transportation of the electrons and ions,⁶² and demonstrates the battery-type nature of the materials.⁶³ A slight shift in the position of the redox peaks was observed which indicates the reversibility and enhanced stability of the electrode's materials. A plausible mechanism that represents redox reaction is presented by equation 8.



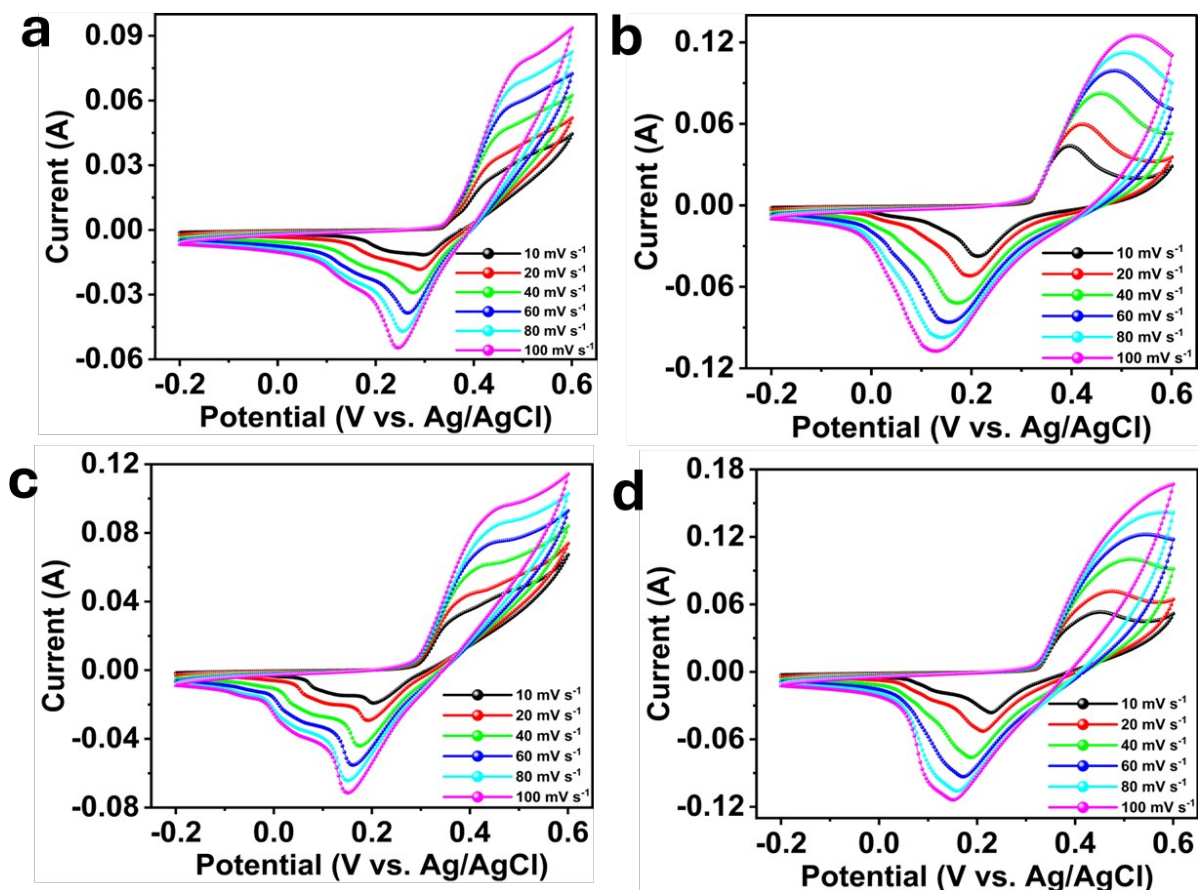


Figure 4. CV profiles of (a) pristine TiO_2 , (b) Er-doped TiO_2 , (c) Eu-doped TiO_2 , and (d) Er/Eu co-doped TiO_2 nanoparticles in 2 M KOH electrolyte.

It is important to note that the charge stored in the electrode is a combination of diffusion-controlled and capacitive phenomena. Therefore, the identification of both processes and their individual contributions is essential to the overall capacity of the electrode materials. At a fixed potential, the relation between the current (i) and scan rate (v) can be represented by a power law equation 9.⁶⁴

$$i = a v^b \quad (9)$$

with the value of b being determined from the slope of $\log(i)$ vs. $\log(v)$ and which can be used to define the charge storage process. For a value of b of 1 or close to it, the charge storage is capacitive in nature, due to surface adsorption/desorption of the electrolyte ions while a value of b of 0.5 or below indicates diffusion-controlled faradaic processes. The b values for pristine, Er-doped, Eu-doped and Er/Eu co-doped TiO_2 materials are 0.32, 0.20, 0.18 and 0.17 respectively which indicates that charge storage in these materials is primarily diffusion-controlled in nature as shown in **Figure S3**.

Furthermore, the quantitative contribution from both the surface and diffusion capacitances of Eu-doped TiO₂ as well as Er/Eu co-doped TiO₂ materials were calculated by Dunn's method using equation 10.⁶⁵

$$i(V) = k_1 v + k_2 v^{\frac{1}{2}} \quad (10)$$

with $k_1 v$ and $k_2 v^{1/2}$ indicating the surface and diffusion capacitances of the materials. Values of k_1 and k_2 were determined from the slope and intercept of the line that result from a plot of $i(V)/v^{1/2}$ vs $v^{1/2}$ at a fixed potential with different currents from the CV as shown in **Figure 5(a, d)**. The diffusion-controlled (green region) and capacitive (red) charge storage contributions were determined at 10 mV s⁻¹ from the CV profiles for Eu-doped TiO₂ and Er/Eu co-doped TiO₂ materials, which were 83% and 86% for diffusion processes and 17% and 14% for capacitive processes, respectively, as shown in **Figure 5(b, e)**. Moreover, the percentage contribution of surface and diffusion capacitances of the materials at varying scan rates were also represented by the bar plots, see **Figure 5(c, f)**. The bar plot shows that at a lower scan rate, the diffusion contribution is higher than that of the surface in each material. This suggests that at lower scan rates the ions have sufficient time to permeate into the inner regions of the electrode. For Eu-doped TiO₂ nanoparticles the diffusion capacitance contributes 83% and the surface 17%, while for Er/Eu co-doped TiO₂ 86% is derived from diffusion and 14% from the surface. The quantitative investigations of surface and diffusion capacitance for pristine TiO₂ and Er-doped TiO₂ nanoparticles are presented in **Figure S4**.

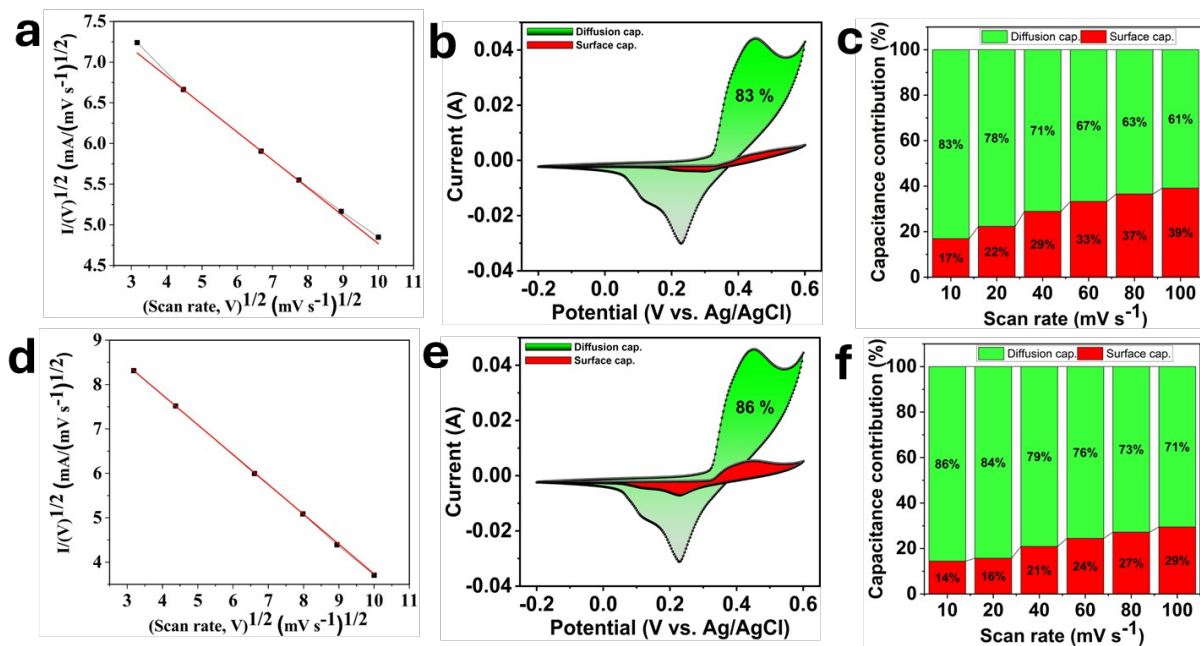


Figure 5. A quantitative analysis of the relative contributions from the surface and diffusion capacitance for Eu-doped TiO₂, and Er/Eu co-doped TiO₂ nanoparticles. (a, d) plots of $(i/v^{1/2})$ vs $(v^{1/2})$ to calculate the values of k_1 and k^2 , (b, e) contribution from diffusion and capacitive currents to the charge storage at 10 mV s^{-1} , (c, f) plots of the ratios of capacitive to diffusion contribution at different scan rates.

Galvanostatic charge-discharge (GCD) curves were conducted for the fabricated electrodes, which demonstrate a non-linear profile which is typical of battery-type behavior, and are displayed in **Figure 6(a, b, c, d)**. The C_{sp} values evaluated for pristine, Er-doped, Eu-doped, and Er/Eu co-doped TiO₂ nanoparticles are 575 F g^{-1} , 910 F g^{-1} , 1215 F g^{-1} , and 1772 F g^{-1} at 1 A g^{-1} , respectively. The high specific capacitance of Er/Eu co-doped TiO₂ compared to other materials is due to the facile transportation of the charges at the electrode-electrolyte interface. This fast charge transport arises due to the co-doping of the Er and Eu metals that create a large number of defects and oxygen vacancies and therefore increase the number of active sites that are responsible for the high performance of the material. The electrode materials demonstrate very high C_{sp} values even at elevated current densities, presented in **Table 1**, which makes them promising materials for supercapacitor applications. In these studies, different potential windows were employed in the CV and GCD investigations in order to avoid water splitting during the charging phenomenon.

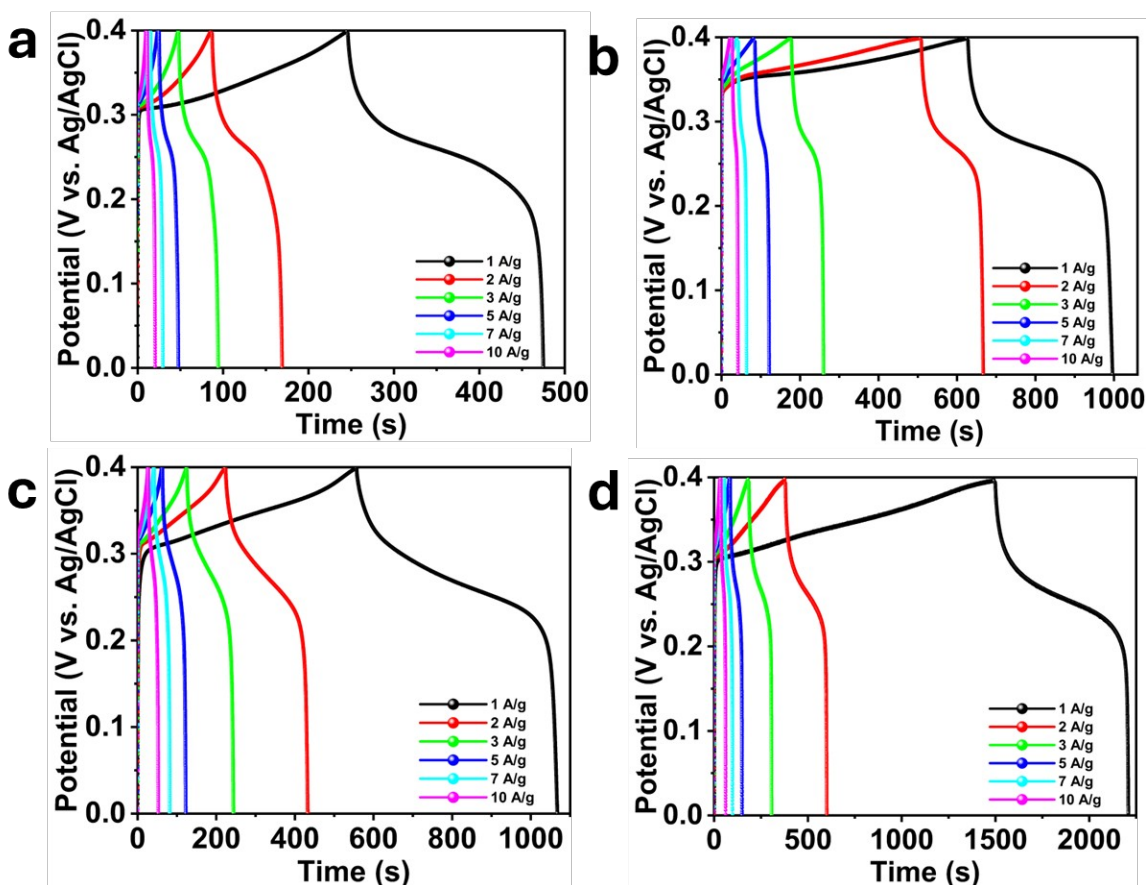


Figure 6. GCD profiles of (a) pristine TiO_2 , (b) Er-doped TiO_2 , (c) Eu-doped TiO_2 , and (d) Er/Eu co-doped TiO_2 nanoparticles

Table 1. Specific capacitance (F g^{-1}) for all four electrodes at different current densities.

Current density (A g^{-1})	1	2	3	5	7	10
TiO_2	575	410	315	282	252	235
Er-doped TiO_2	910	775	615	460	382	370
Eu-doped TiO_2	1215	1020	960	938	893	826
Er/Eu-co-doped TiO_2	1773	1100	908	795	739	654

The Ragone plot in **Figure 7(a)** represents the relation of energy densities to the power density for all the electrodes at different current densities. It is clear from the plot that at lower current densities the energy density of Er/Eu co-doped TiO_2 is much higher than any of the synthesized materials.

To study the charge transfer dynamic of the fabricated electrodes, electrochemical impedance spectroscopy (EIS) was performed at open circuit potential (OCP). The Nyquist plots show a small semicircle in the low frequency region with steep linear behaviour in the higher

frequency region as depicted in **Figure 7(b)**. Er and Eu co-doped TiO₂ possess an extremely small charge transfer resistance (R_{ct}) compared to the other materials which suggest rapid transportation of electrons and ions at the interface of the electrode. The R_{ct} values calculated for the pristine, Er-doped, Eu-doped and Er/Eu co-doped oxides are 376.1 Ω , 120.4 Ω , 83.6 Ω , and 12.37 Ω , however, the solution resistance (R_s) values are 1.120 Ω , 1.097 Ω , 1.091 Ω , and 0.901 Ω , respectively. The R_s is a combination of contributions from the electrolyte, internal, and contact resistances and can be evaluated from the intercept of the EIS profile with the X-axis. A decrease in the R_{ct} value for Er/Eu co-doped TiO₂ was observed which can be attributed to the higher conductivity of the material after co-doping by the transition metal ions. A constant phase element (CPE) with diffusion has been introduced as a component for the equivalent circuit model fitting which is presented as an inset within **Figure 7(b)**. A CPE was selected to represent various factors within the system such as intercalation/deintercalation, active diffusion, the uneven nature of the interface, relaxation times, and most importantly the porosity of the fabricated electrode.⁶⁶ The Bode plots also display the superlative capacitive behavior of the materials, as can be seen from **Figure S5**.

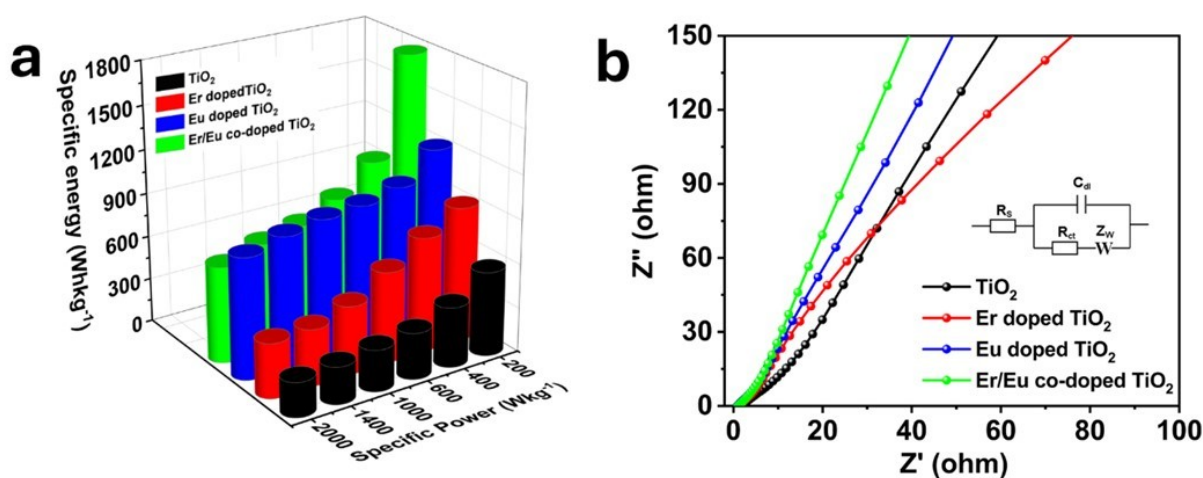


Figure 7. (a) Ragone plot and (b) EIS of all the electrode

Electrochemical Investigation of Asymmetric Device

An asymmetric supercapacitor (ASC) device was assembled by using the best performing material, Er/Eu co-doped TiO₂, as the cathode and activated carbon (AC) as the anode to combine the distinct advantages offered by the two different types of electrode materials. The Er/Eu co-doped TiO₂ electrode undergoes reversible faradaic reactions which contribute to higher energy storage through redox processes, while AC operates through electrostatic charge accumulation, ensuring high power output and long cycle life. Thus, an asymmetric

configuration provides a balanced trade-off between energy density and power density, overcoming the limitations of conventional symmetric supercapacitors which are often constrained by their narrow potential windows and lower energy densities.

Due to the significantly lower specific capacitance of AC, it cannot store charge equal to Er/Eu co-doped TiO₂ and the mass of the active materials at the negative and positive electrodes must be balanced to obtain maximum efficiency. The mass balancing was accomplished by using the formula given in equation 11.

$$\frac{m_+}{m_-} = \frac{C_- \Delta V_-}{C_+ \Delta V_+} \quad (11)$$

3 mg Er/Eu co-doped TiO₂ and 10.6 mg of AC were deposited on a 1.5 cm × 1.5 cm nickel foam substrate separately which were subsequently employed as the positive and the negative electrode, respectively. The CV profiles of the device were recorded in a potential window of 0 to +1.6 V at a scan rate of 10 to 100 mV s⁻¹ in 2 M KOH electrolyte in **Figure 8(a)**. The GCD curves of the device are triangular in shape which indicates the superior reversibility of the device (see **Figure 8(b)**). The C_{sp} values evaluated for devices are 135, 116.25, 110.62, 78.75, and 51.87 F g⁻¹ at 2, 3, 5, 7, and 10 A g⁻¹, respectively. The energy and power densities of the device were calculated from the Ragone plot as displayed in **Figure 8(c)**. The Er/Eu co-doped TiO₂ exhibits the maximum energy density of 48 Wh kg⁻¹ at a power density of 1.6 kW kg⁻¹ when measured at 2 A g⁻¹. The charge storage capacity and excellent reversibility of the asymmetric device was estimated through the capacity retention and coulombic efficiency.⁶⁷⁻⁶⁸ The device was subjected to prolonged coulombic cycling and it was found that the device was very stable with a capacitance retention of 95.4% and coulombic efficiency of 98.68 % after 6000 cycles as shown in **Figure 8(d)**.

Nyquist plots were used to evaluate R_{ct} and R_s of the fabricated device by applying the fitting model circuit, see inset of **Figure 8(e)**. A suppressed arc has been observed in the higher frequency region, which can be due to polarization of the device, with a straight line at higher frequency that was less than a 90° angle to the real axis because of the mass transfer effect and represents the Warburg impedance. Nyquist plots were conducted in the frequency range of 0.1 Hz to 100 kHz at the highest operating voltage of 1.6 V. The R_{ct} and R_s values are 8.394 Ω and 1.066 Ω as calculated using a CPE with diffusion model. Furthermore, the asymmetric device was first charged to a potential of 1.6 V, the power turned off and the OCP as a function of time assessed, see **Figure 8(f)**. The self-discharge curve showed a sharp

discharge rate until a value of 0.8 V was reached after which the potential remains relatively constant.

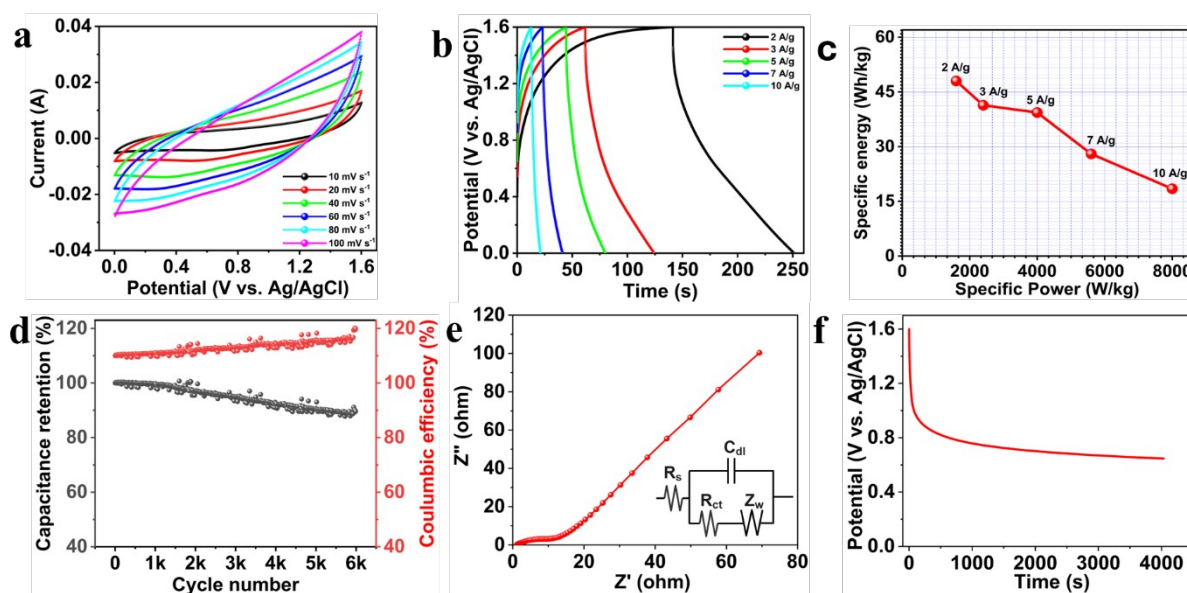


Figure 8. Electrochemical study of asymmetric supercapacitor. (a) CV curves at varying scan rates (b) GCD profiles at different current densities (c) Ragone plot (d) Cyclic stability (e) EIS profile with model fitting, and (f) Self-discharge test.

Electrochemical OER Investigations

To determine the potential at which the OER reaction occurs as well as the overpotential the as-synthesized materials were evaluated by linear sweep voltammetry (LSV).⁶⁹ All measurements were carried out at a constant scan rate of 5 mV s^{-1} in 1 M KOH solution. The iR uncompensated LSV curves of TiO_2 , Er-doped TiO_2 , Eu-doped TiO_2 and Er/Eu co-doped TiO_2 materials are displayed in **Figure 9(a)**. Generally, researchers have reported OER potential at a current density of 10 mA cm^{-2} while reason for reporting the OER potential at 20 mA cm^{-2} is due to the presence of redox peaks in a similar potential region. The values calculated for the OER onset potential for pristine TiO_2 , Er-doped TiO_2 , Eu-doped TiO_2 , and Er/Eu co-doped TiO_2 materials in this study are 1.58, 1.53, 1.50 and 1.48 V respectively and the calculated overpotential (η) values were 470, 430, 400 and 330 mV, respectively. The Er/Eu co-doping in TiO_2 creates structural defects which ultimately supports the rapid transfer of electrons and boosts the electrochemical water splitting of the materials. The electrolysis of water has been carried out in the solution phase which always possesses R_s and which can be evaluated from the Nyquist plots obtained by EIS.⁷⁰ EIS was conducted at OCP to obtain Nyquist plots which are presented in **Figure 9(b)**. The values of R_s calculated for pristine TiO_2 , Er-doped TiO_2 , Eu-doped, and Er/Eu co-doped TiO_2 materials are 2.923, 2.712,

2.291, and 1.851 Ω , respectively. The obtained R_s values were then used to obtain a 100% iR potential drop.⁷¹

Moreover, the 100% iR corrected LSV profiles of pristine TiO₂, Er-doped TiO₂, Eu-doped TiO₂ and Er/Eu co-doped TiO₂ show lower values for the onset potential compared to the iR uncompensated values as presented in **Figure 9(c)**. The calculated onset potentials for pristine TiO₂, Er-doped TiO₂, Eu-doped TiO₂, and Er/Eu co-doped TiO₂ are 1.58, 1.52, 1.49 and 1.47 V respectively. On the other hand, overpotential values estimated for pristine TiO₂, Er-doped TiO₂, Eu-doped TiO₂, and Er/Eu co-doped TiO₂ were 460, 400, 380 and 290 mV at 20 mA cm⁻².

Another important aspect that determines the performance of catalysts with respect to the OER electrolysis are the kinetic parameters.⁷² To determine the kinetic parameters of the electrocatalysts, Tafel analysis was employed and the Tafel slopes calculated were 166.11, 164.71, 139.08 and 115.19 mV dec⁻¹ for pristine TiO₂, Er-doped TiO₂, Eu-doped TiO₂ and Er/Eu co-doped TiO₂, respectively (see **Figure 9(d)**). The Er/Eu co-doped TiO₂ catalyst demonstrates a lower Tafel slope value which suggests the presence of facile kinetics for this potential catalyst. Together, the electrochemical investigations as well as the Tafel slope value for Er/Eu co-doped TiO₂ indicate that it is the most efficient electrocatalyst among all the materials reported here. Additionally, the TOF was calculated at an overpotential of 350 mV the values of which were found to be 0.69, 3.97, 4.01 and 13.76 for pristine TiO₂, Er-doped TiO₂, Eu-doped TiO₂ and Er/Eu co-doped TiO₂, respectively. The electrochemical durability of the electrocatalyst is an important performance parameter and has been tested for the Eu-doped, and Er/Eu co-doped TiO₂ catalysts at a fixed potential of 1.65 V (vs. RHE), with the potential curve presented in **Figure 9(e)**, where it can be seen that both materials demonstrate excellent stability. The stable current density of 50 and 45 mA/cm² for Eu-doped TiO₂ and Er/Eu co-doped TiO₂ catalysts respectively over a 20 hour period demonstrated that the reported catalysts are indeed stable for practical water electrolysis.

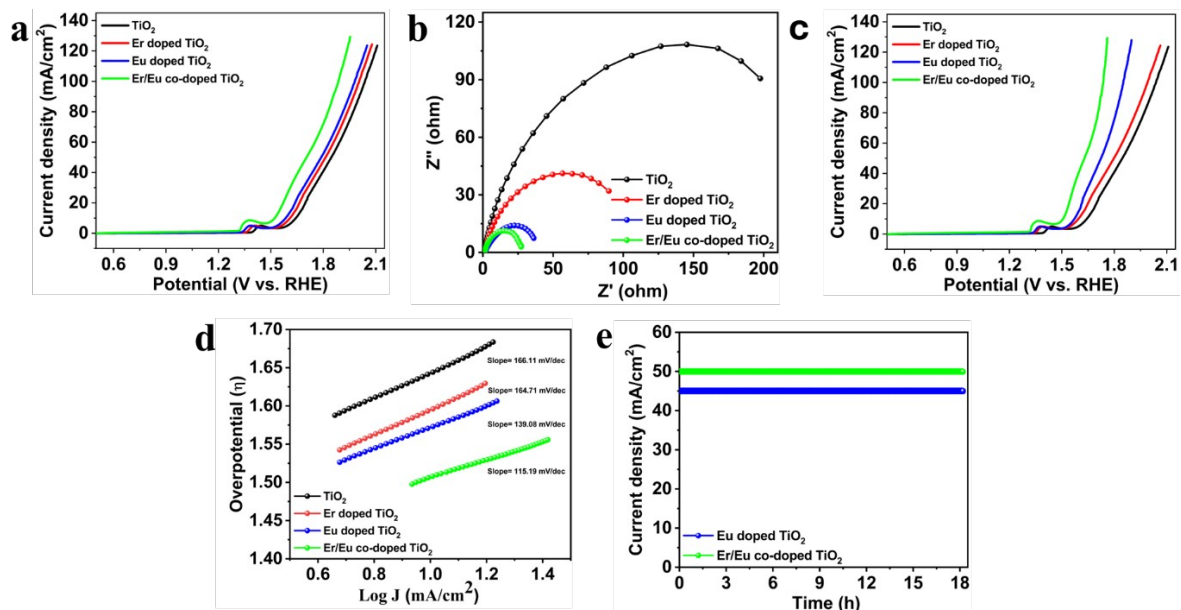


Figure 9. (a) Uncompensated LSV profiles, (b) EIS, (c) iR compensated LSV profiles, (d) Tafel plot with values of the slopes, (e) control potential analysis of Eu-doped TiO_2 and Er/Eu co-doped TiO_2 electrocatalysts for OER.

Conclusion.

Pristine TiO_2 , Er-doped, Eu-doped, and Er/Eu co-doped TiO_2 nanoparticles have been synthesized using simple solution chemistry. Among all the fabricated electrodes, Er/Eu co-doped TiO_2 showed the highest specific capacitance of 1772.5 F g^{-1} at 1 A g^{-1} and low R_{ct} of $12.37 \text{ } \Omega$, highlighting an enhanced electrical conductivity and rapid ion and electron transport. The Er/Eu co-doped TiO_2 was further explored as a material for supercapacitor applications in an asymmetric device and was found to possess a wide potential window of 1.6 V , specific capacitance of 135 F g^{-1} at 2 A g^{-1} , an energy density of 48 Wh kg^{-1} , and a power density of 1.6 kW kg^{-1} . Additionally, the pristine TiO_2 , Er-doped, Eu-doped and Er/Eu co-doped TiO_2 materials exhibited an excellent oxygen evolution reaction performance, with onset potentials of 1.57 , 1.52 , 1.49 and 1.47 V , and low overpotentials of 460 , 400 , 380 and 290 mV at 20 mA cm^{-2} . The outstanding feature of this work is the remarkable electrochemical stability of the electrocatalysts when tested for a period of 20 hours using constant potential electrolysis. Tafel plot slopes of 166.11 , 164.71 , 139.08 and $115.19 \text{ mV dec}^{-1}$, suggest that all these electrocatalysts are cutting-edge materials for OER research. These results demonstrate that Er/Eu co-doped TiO_2 is a promising electrode material for supercapacitors. Additionally, these catalysts, which do not use precious metals, offer significant insights into the development of new materials for water splitting.

Acknowledgements

MNH and SH gratefully acknowledge the Commonwealth Scholarship Commission (CSC) for financial support through the Split-Site programme (PKCN-2019-175).

Author Contributions

MNH and AB contributed equally to this work.

References

1. Xiao, Z.; Wang, R.; Jiang, D.; Qian, Z.; Li, Y.; Yang, K.; Sun, Y.; Zeng, Z.; Wu, F., Recent developments of two-dimensional anode materials and their composites in lithium-ion batteries. *ACS Appl. Energy Mater.* **2021**, 4 (8), 7440-7461.
2. Deng, L.; Wang, Y.; Li, D.; Ni, X.; Ju, A., FeCoO Nanosheet Grown on Free-Standing Carbon Fiber Paper for Boosting the Oxygen Evolution Reaction and Lithium-Ion Batteries. *ACS Appl. Energy Mater.* **2024**.
3. Dar, M. A.; Majid, S.; Satgunam, M.; Siva, C.; Ansari, S.; Arusalan, P.; Ahamed, S. R., Advancements in Supercapacitor electrodes and perspectives for future energy storage technologies. *Int. J. Hydrogen Energy* **2024**, 70, 10-28.
4. Oyedotun, K. O.; Mamba, B. B., New trends in supercapacitors applications. *Inorg. Chem. Commun.* **2024**, 113154.
5. Kumar, Y. A.; Roy, N.; Ramachandran, T.; Hussien, M.; Moniruzzaman, M.; Joo, S. W., Shaping the future of energy: The rise of supercapacitors progress in the last five years. *J. Energy Storage* **2024**, 98, 113040.
6. Zhang, Y.; Li, L.; Su, H.; Huang, W.; Dong, X., Binary metal oxide: advanced energy storage materials in supercapacitors. *J. Mater. Chem.* **2015**, 3 (1), 43-59.
7. Gonçalves, J. M.; da Silva, M. I.; Silva, M. N.; Martins, P. R.; Nossol, E.; Toma, H. E.; Angnes, L., Recent progress in ZnCo₂O₄ and its composites for energy storage and conversion: a review. *Energy Advances* **2022**, 1 (11), 793-841.
8. Conway, B. E.; Birss, V.; Wojtowicz, J., The role and utilization of pseudocapacitance for energy storage by supercapacitors. *J. Power Sources* **1997**, 66 (1-2), 1-14.
9. Zheng, J. P.; Huang, J.; Jow, T. R., The Limitations of Energy Density for Electrochemical Capacitors. *JES* **1997**, 144 (6), 2026.
10. Sun, K.; Wang, L.; Wang, Z.; Wu, X.; Fan, G.; Wang, Z.; Cheng, C.; Fan, R.; Dong, M.; Guo, Z., Flexible silver nanowire/carbon fiber felt metacomposites with weakly negative permittivity behavior. *PCCP* **2020**, 22 (9), 5114-5122.
11. Sun, K.; Fan, R.; Yin, Y.; Guo, J.; Li, X.; Lei, Y.; An, L.; Cheng, C.; Guo, Z., Tunable negative permittivity with fano-like resonance and magnetic property in percolative silver/yttrium iron garnet nanocomposites. *J. Phys. Chem. C* **2017**, 121 (13), 7564-7571.
12. Raj, C. C.; Prasanth, R., advent of TiO₂ nanotubes as supercapacitor electrode. *JES* **2018**, 165 (9), E345.
13. Yang, W.; Gao, Z.; Wang, J.; Wang, B.; Liu, Q.; Li, Z.; Mann, T.; Yang, P.; Zhang, M.; Liu, L., Synthesis of reduced graphene nanosheet/urchin-like manganese dioxide composite and high performance as supercapacitor electrode. *Electrochim. Acta* **2012**, 69, 112-119.
14. Zhang, L. L.; Zhao, X., Carbon-based materials as supercapacitor electrodes. *Chem Soc Rev* **2009**, 38 (9), 2520-2531.

15. Liang, R.; Du, Y.; Xiao, P.; Cheng, J.; Yuan, S.; Chen, Y.; Yuan, J.; Chen, J., Transition metal oxide electrode materials for supercapacitors: a review of recent developments. *Nanomater.* **2021**, 11 (5), 1248.
16. Hussain, M. N.; Inayat, A.; Ansir, R.; Naveed, A.; Abbas, S. M.; Haider, A.; Shah, S. M., Probing the Synergy of Ni(OH)₂/NiO Nanoparticles Supported on rGO for Battery-Type Supercapacitors. *Energy Technol.* **2024**, 12 (2), 2300854.
17. Huang, R.; Zhang, J.; Dong, Z.; Lin, H.; Han, S., Oxygen vacancy engineering of TiO₂/WO₃ composites on a carbon fiber as advanced electrodes for high-performance flexible supercapacitors. *ACS Appl. Energy Mater.* **2023**, 6 (3), 1673-1684.
18. Wu, J.; Huang, F.; Lee, T.; Yan, Y.; Pei, X.; Wang, M.; Gao, S.; Guo, S.; Pan, X.; Wang, P., Interface-guided formation of 2D ultrathin MnO₂ nanosheets with abundant oxygen defects for high performance supercapacitors. *ACS Appl. Energy Mater.* **2022**, 5 (6), 6962-6969.
19. Wang, N.; Zhao, P.; Liang, K.; Yao, M.; Yang, Y.; Hu, W., CVD-grown polypyrrole nanofilms on highly mesoporous structure MnO₂ for high performance asymmetric supercapacitors. *J. Chem. Eng.* **2017**, 307, 105-112.
20. Lu, X.; Yu, M.; Wang, G.; Zhai, T.; Xie, S.; Ling, Y.; Tong, Y.; Li, Y., H-TiO₂@MnO₂//H-TiO₂@ C core-shell nanowires for high performance and flexible asymmetric supercapacitors. *Adv. Mater* **2013**, 25 (2), 267-272.
21. Lu, X.; Wang, G.; Zhai, T.; Yu, M.; Gan, J.; Tong, Y.; Li, Y., Hydrogenated TiO₂ nanotube arrays for supercapacitors. *Nano lett.* **2012**, 12 (3), 1690-1696.
22. Hanaor, D. A.; Sorrell, C. C., Review of the anatase to rutile phase transformation. *J. Mater. Sci.* **2011**, 46, 855-874.
23. Zhang, H.; Banfield, J. F., Thermodynamic analysis of phase stability of nanocrystalline titania. *J. Mater. Chem.* **1998**, 8 (9), 2073-2076.
24. Kisch, H.; Zang, L.; Lange, C.; Maier, W. F.; Antonius, C.; Meissner, D., Modified, amorphous titania—a hybrid semiconductor for detoxification and current generation by visible light. *Angew. Chem., Int. Ed.* **1998**, 37 (21), 3034-3036.
25. Chang, S.-m.; Doong, R.-a., Characterization of Zr-doped TiO₂ nanocrystals prepared by a nonhydrolytic sol-gel method at high temperatures. *JPC B* **2006**, 110 (42), 20808-20814.
26. Ojha, D. P.; Poudel, M. B.; Kim, H. J., Investigation of electrochemical performance of a high surface area mesoporous Mn doped TiO₂ nanoparticle for a supercapacitor. *Mater. Lett.* **2020**, 264, 127363.
27. Liu, Q.; Yang, Y.; Ni, Y.; Wang, Q.; Yu, H.; Zhu, X.; Ying, Z.; Song, Y., A general approach to the fabrication of Sn-doped TiO₂ nanotube arrays with titanium vacancies for supercapacitors. *Appl. Surf. Sci.* **2021**, 570, 151175.
28. Jiang, L.; Tian, H.; Shen, W.; Wang, Y.; Ma, Y.; Hou, P.; Wu, Y.; Xiang, P.; Xiao, T.; Tan, X., N-doped TiO₂ hierarchical microspheres as electrode for high-performance supercapacitors. *Mater. Lett.* **2021**, 295, 129840.
29. Appadurai, T.; Subramaniam, C. M.; Kuppusamy, R.; Karazhanov, S.; Subramanian, B., Electrochemical performance of nitrogen-doped TiO₂ nanotubes as electrode material for supercapacitor and Li-ion battery. *Molecules* **2019**, 24 (16), 2952.
30. Li, C.; Wang, Z.; Li, S.; Cheng, J.; Zhang, Y.; Zhou, J.; Yang, D.; Tong, D.-G.; Wang, B., Interfacial engineered polyaniline/sulfur-doped TiO₂ nanotube arrays for ultralong cycle lifetime fiber-shaped, solid-state supercapacitors. *ACS Appl. Mater. Interfaces.* **2018**, 10 (21), 18390-18399.
31. Wang, L.; Yang, H.; Shu, T.; Xin, Y.; Chen, X.; Li, Y.; Li, H.; Hu, X., Nanoengineering S-doped TiO₂ embedded carbon nanosheets for pseudocapacitance-enhanced Li-ion capacitors. *ACS Appl. Energy Mater* **2018**, 1 (4), 1708-1715.

32. Hussain, M. N.; Naveed, A.; Inayat, A.; Bilal, M.; Haider, A.; Shah, S. M., Investigating the Impact of Ag Nanoparticles on N and S Co-Doped TiO₂ for Battery-Type Supercapacitor Application. *ChemistrySelect* **2023**, 8 (48), e202303224.
33. Jaffri, S. B.; Ahmad, K. S.; Abrahams, I.; Karim, M. R., Synergistic (Ce/Pr/Nd) 3⁺-doped TiO₂ hetero-system as bifunctional catalyst, electrode material, and electron conveyance layer in perovskite solar cells. *Int. J. Hydrogen Energy* **2024**, 71, 1392-1404.
34. Munawar, T.; Manzoor, S.; Jabbour, K.; Nisa, M. U.; Sardar, S.; Mukhtar, F.; Osman, S. M.; Esan, M. F.; Ashiq, M. N.; Iqbal, F., Nanostructural engineered titanium dioxide by rare earth metals dual doping for electrochemical supercapacitor applications. *J. Korean Ceram. Soc.* **2024**, 1-13.
35. Li, Y.; Ni, G.; Zhang, K.; Wang, D.; Li, Q.; Wang, S., Construction of 3D N-doped Ti₃C₂/TiO₂ hollow sphere structure with superior electrochemical performance for supercapacitor. *J. Alloys Compd.* **2024**, 970, 172526.
36. Sun, Y.; Zhao, Z.; Li, P.; Li, G.; Chen, Y.; Zhang, W.; Hu, J., Er-doped ZnO nanofibers for high sensibility detection of ethanol. *Appl. Surf. Sci.* **2015**, 356, 73-80.
37. Yang, Y.; Pu, H.; Di, J.; Zang, Y.; Zhang, S.; Chen, C., Synthesis and characterization of monolayer Er-doped MoS₂ films by chemical vapor deposition. *Scr. Mater.* **2018**, 152, 64-68.
38. Yang, J.; Hu, Y.; Jin, C.; Zhuge, L.; Wu, X., Structural and optical properties of Er-doped TiO₂ thin films prepared by dual-frequency magnetron co-sputtering. *Thin Solid Films* **2017**, 637, 9-13.
39. Trandafilović, L. V.; Jovanović, D. J.; Zhang, X.; Ptasińska, S.; Dramićanin, M., Enhanced photocatalytic degradation of methylene blue and methyl orange by ZnO: Eu nanoparticles. *Appl. Catal. B: Environ* **2017**, 203, 740-752.
40. Phuruangrat, A.; Cheed-Im, U.; Thongtem, T.; Thongtem, S., High visible light photocatalytic activity of Eu-doped MoO₃ nanobelts synthesized by hydrothermal method. *Mater. Lett.* **2016**, 172, 166-170.
41. Su, B.; Wang, S.; Yang, W.; Wang, Y.; Huang, L.; Popat, K. C.; Kipper, M. J.; Belfiore, L. A.; Tang, J., Synthesis of Eu-modified luminescent Titania nanotube arrays and effect of voltage on morphological, structural and spectroscopic properties. *Mater. Sci. Semicond. Process.* **2020**, 113, 105026.
42. Jin, L.; Li, G.; Liu, B.; Li, Z.; Zheng, J.; Zheng, J. P., A novel strategy for high-stability lithium sulfur batteries by in situ formation of polysulfide adsorptive-blocking layer. *J. Power Sources* **2017**, 355, 147-153.
43. Lin, H.; Zhang, M.; Miao, J.; Li, L.; Xin, K.; Liao, X.; Feng, Z., Synthesis and electrochemical properties of Er/ α -MnO₂ microspheres for supercapacitors application. *Ionics* **2019**, 25 (8), 3867-3873.
44. Hu, Q.; Yue, B.; Yang, F.; Shao, H.; Bao, M.; Wang, Y.; Liu, J., Electrochemical and magnetic properties of perovskite type RMnO₃ (R= La, Nd, Sm, Eu) nanofibers. *J. Alloys Compd.* **2021**, 872, 159727.
45. Portia, S. A. U.; Srinivasan, R.; Elaiyappillai, E.; Johnson, P. M.; Ramamoorthy, K., Facile synthesis of Eu-doped CaTiO₃ and their enhanced supercapacitive performance. *Ionics* **2020**, 26, 3543-3554.
46. Aghazadeh, M.; Karimzadeh, I., Fabrication of high-performance metal ion doped iron oxide electrode for supercapacitor applications through a novel platform. *Mater. Res. Express* **2017**, 4 (10), 105505.
47. Shunmughanathan, B.; Dheivasigamani, T.; Pitchai, J. S. K., Rare-earth gallium garnet (RE₃Ga₅O₁₂, RE= Eu, Gd, Dy, Er, and Yb) self-assembled nanostructure based

- battery type electrodes for efficient asymmetric supercapacitor applications. *J. Energy Storage* **2023**, *73*, 109092.
48. Bashir, A.; Inayat, A.; Bashir, R.; Jamil, S.; Abbas, S. M.; Sultan, M.; Iqbal, A.; Akhter, Z., Design of porous Ni and rare earth metal (Ce, Ho, and Eu) Co-doped TiO₂ nanoarchitectures for energy conversion and storage applications. *New J Chem* **2023**, *47* (7), 3560-3571.
 49. Suen, N.-T.; Hung, S.-F.; Quan, Q.; Zhang, N.; Xu, Y.-J.; Chen, H. M., Electrocatalysis for the oxygen evolution reaction: recent development and future perspectives. *Chem Soc Rev* **2017**, *46* (2), 337-365.
 50. Swaminathan, J.; Subbiah, R.; Singaram, V., Defect-Rich Metallic Titania (TiO_{1.23})□ An Efficient Hydrogen Evolution Catalyst for Electrochemical Water Splitting. *ACS Catal.* **2016**, *6* (4), 2222-2229.
 51. Tahir, A.; Zubair, U.; Rafique, F.; Munir, A.; Haik, Y.; Hussain, I.; ur Rehman, H., Au/TiO₂ thin film with ultra-low content of gold: an efficient self-supported bifunctional electrocatalyst for oxygen and hydrogen evolution reaction. *Catal. Today* **2023**, *418*, 114078.
 52. Munir, S.; Shah, S. M.; Hussain, H., Effect of carrier concentration on the optical band gap of TiO₂ nanoparticles. *Mater. Des.* **2016**, *92*, 64-72.
 53. Sun, H.; Pan, J.; Yan, X.; Shen, W.; Zhong, W.; Cheng, X., MnO₂ nanoneedles loaded on silicon oxycarbide-derived hierarchically porous carbon for supercapacitor electrodes with enhanced electrochemical performance. *Ceram. Int.* **2019**, *45* (18), 24802-24810.
 54. Khan, N. A.; Ahmad, I.; Rashid, N.; Hussain, S.; Zairov, R.; Alsaiani, M.; Alkorbi, A. S.; Ullah, Z.; Nazar, M. F., Effective CuO/CuS heterostructures catalyst for OER performances. *Int. J. Hydrogen Energy* **2023**, *48* (80), 31142-31151.
 55. Ma, Y.; Zhang, J.; Tian, B.; Chen, F.; Wang, L., Synthesis and characterization of thermally stable Sm, N co-doped TiO₂ with highly visible light activity. *J. Hazard. Mater.* **2010**, *182* (1-3), 386-393.
 56. Xin, B.; Ren, Z.; Wang, P.; Liu, J.; Jing, L.; Fu, H., Study on the mechanisms of photoinduced carriers separation and recombination for Fe³⁺-TiO₂ photocatalysts. *Appl. Surf. Sci.* **2007**, *253* (9), 4390-4395.
 57. Zhou, H.; Chen, Q.; Li, G.; Luo, S.; Song, T.-b.; Duan, H.-S.; Hong, Z.; You, J.; Liu, Y.; Yang, Y., Interface engineering of highly efficient perovskite solar cells. *Science* **2014**, *345* (6196), 542-546.
 58. Gao, X.-X.; Ge, Q.-Q.; Xue, D.-J.; Ding, J.; Ma, J.-Y.; Chen, Y.-X.; Zhang, B.; Feng, Y.; Wan, L.-J.; Hu, J.-S., Tuning the fermi-level of TiO₂ mesoporous layer by lanthanum doping towards efficient perovskite solar cells. *Nanoscale* **2016**, *8* (38), 16881-16885.
 59. Al Kiey, S. A.; Abdelhamid, H. N., Metal-organic frameworks (MOFs)-derived Co₃O₄@ N-doped carbon as an electrode materials for supercapacitor. *J. Energy Storage* **2022**, *55*, 105449.
 60. Xia, T.; Zhang, X.; Zhao, J.; Li, Q.; Ao, C.; Hu, R.; Zheng, Z.; Zhang, W.; Lu, C.; Deng, Y., Flexible and conductive carbonized cotton fabrics coupled with a nanostructured Ni(OH)₂ coating for high performance aqueous symmetric supercapacitors. *ACS Sustain. Chem. Eng.* **2019**, *7* (5), 5231-5239.
 61. Yang, S.; Lin, Y.; Song, X.; Zhang, P.; Gao, L., Covalently coupled ultrafine H-TiO₂ nanocrystals/nitrogen-doped graphene hybrid materials for high-performance supercapacitor. *ACS Appl. Mater. Interfaces.* **2015**, *7* (32), 17884-17892.

62. Ma, Y.; Bai, Y.; Liang, B.; Yang, R.; Jiang, X.; Zheng, S.; Zhang, C.; Hu, C., Doping-induced morphology modulation for boosting the capacity and stability of nanocrystals assembled $\text{Ni}_{1-x}\text{Co}_x\text{Se}_2$. *Appl. Surf. Sci.* **2022**, 579, 152156.
63. Liu, Y.; Fu, N.; Zhang, G.; Xu, M.; Lu, W.; Zhou, L.; Huang, H., Design of Hierarchical $\text{Ni} \square \text{Co} @ \text{Ni} \square \text{Co}$ Layered Double Hydroxide Core–Shell Structured Nanotube Array for High-Performance Flexible All-Solid-State Battery-Type Supercapacitors. *Adv. Funct. Mater.* **2017**, 27 (8), 1605307.
64. Mariappan, V. K.; Krishnamoorthy, K.; Pazhamalai, P.; Sahoo, S.; Kim, S.-J., Electrodeposited molybdenum selenide sheets on nickel foam as a binder-free electrode for supercapacitor application. *Electrochim. Acta* **2018**, 265, 514-522.
65. Pazhamalai, P.; Krishnamoorthy, K.; Mariappan, V. K.; Kim, S.-J., Blue TiO_2 nanosheets as a high-performance electrode material for supercapacitors. *J. Colloid Interface Sci* **2019**, 536, 62-70.
66. Pandit, B.; Pande, S. A.; Sankapal, B. R., Facile SILAR processed Bi_2S_3 : pbS solid solution on MWCNTs for high-performance electrochemical supercapacitor. *Chin. J. Chem.* **2019**, 37 (12), 1279-1286.
67. Tahir, M.; He, L.; Li, L.; Cao, Y.; Yu, X.; Lu, Z.; Liao, X.; Ma, Z.; Song, Y., Pushing the electrochemical performance limits of polypyrrole toward stable microelectronic devices. *Nanomicro Lett* **2023**, 15 (1), 49.
68. Tahir, M.; Li, L.; He, L.; Xiang, Z.; Ma, Z.; Haider, W. A.; Liao, X.; Song, Y., Interdigital $\text{MnO}_2/\text{PEDOT}$ Alternating Stacked Microelectrodes for High-Performance On-Chip Microsupercapacitor and Humidity Sensing. *Energy Environ. Mater.* **2024**, 7 (2), e12546.
69. Sohail, M.; Ayyob, M.; Wang, A.; Altuijri, R.; El Maati, L. A.; Ahmad, I., Revolutionizing water oxidation: NiSe/NiO heterostructure as a high-performing oxygen evolution reaction catalyst. *Int. J. Hydrogen Energy* **2024**, 51, 1042-1049.
70. García-Osorio, D.; Jaimes, R.; Vazquez-Arenas, J.; Lara, R.; Alvarez-Ramirez, J., The kinetic parameters of the oxygen evolution reaction (OER) calculated on inactive anodes via EIS transfer functions: $\bullet\text{OH}$ formation. *JES* **2017**, 164 (11), E3321.
71. Khan, N. A.; Rashid, N.; Ahmad, I.; Zairov, R.; ur Rehman, H.; Nazar, M. F.; Jabeen, U., An efficient $\text{Fe}_2\text{O}_3/\text{FeS}$ heterostructures water oxidation catalyst. *Int. J. Hydrogen Energy* **2022**, 47 (53), 22340-22347.
72. van der Heijden, O.; Park, S.; Eggebeen, J. J.; Koper, M. T., Non-kinetic effects convolute activity and Tafel analysis for the alkaline oxygen evolution reaction on NiFeOOH electrocatalysts. *Angew. Chem., Int. Ed.* **2023**, 62 (7), e202216477.